

Article

Structure and Composition of Micro-Manganese Nodules in Deep-Sea Carbonate from the Zhaoshu Plateau, North of the South China Sea

Hengchao Xu ¹, Xiaotong Peng ^{1,*}, Kaiwen Ta ¹, Taoran Song ², Mengran Du ¹, Jiwei Li ¹, Shun Chen ^{1,3} and Zhiguo Qu ¹

¹ Institute of Deep Sea Science and Engineering, Chinese Academy of Sciences, Sanya 572000, China; hcxu@idsse.ac.cn (H.X.); takaiwen@idsse.ac.cn (K.T.); mdu@idsse.ac.cn (M.D.);

lijjwei20025@idsse.ac.cn (J.L.); chans@idsse.ac.cn (S.C.); quzhiguo@idsse.ac.cn (Z.Q.)

² College of Marine Science and Technology, Hainan Tropical Ocean University, Sanya 572000, China; trqyx1221@163.com

³ Southern Marine Science and Engineering Guangdong Laboratory (Zhuhai), Zhuhai 519000, China

* Correspondence: xtpeng@idsse.ac.cn; Tel.: +86-0898-8838-0172

Received: 23 September 2020; Accepted: 11 November 2020; Published: 15 November 2020



Abstract: The occurrence of deep-sea ferromanganese nodules and crusts on the seafloor is widespread, providing an important resource for numerous metals such as Ni, Co, and Cu. Although they have been intensively studied in the past, the formation of micro-manganese nodules within carbonate rocks has received less attention, despite the considerable amounts of manganese released from the dissolution of the calcareous framework. The micro-petrographic and geochemical characteristics of reef carbonate rocks recovered from the Zhaoshu plateau in the Xisha uplift, north of the South China Sea, were studied using optical microscopy, scanning electron microscopy, confocal Raman spectrometry, and an electron probe micro-analyzer. The carbonate rocks are composed of biogenic debris, including frameworks of coralline algae and chambers of foraminifer, both of which are suffering strong micritization. Within the calcite micrite, numerous micro-manganese nodules were identified with laminated patterns. Mineral and elemental evidence showed that the Mn oxides in the carbonates are mixed with 10 Å vernadite, 7 Å vernadite and todorokite, both of which are closely associated with the carbonate matrix. The micro-nodules were found to have high Mn/Fe ratios, enriched in Ni and Cu and depleted in Co. We infer that these nodules are mixed type with early diagenetic growth under oxic–suboxic conditions. The re-distribution of manganite within the rocks is likely influenced by micritization of the calcareous framework. We deduce that microbial-associated reduction of manganite induces the formation of diagenetic todorokite similar to nodules buried in marine sediments.

Keywords: deep-sea carbonate; micro-manganese nodules; diageneses; South China Sea

1. Introduction

Marine ferromanganese (Fe–Mn) crusts and nodules are found in a variety of marine settings, enriched by several metals, such as Mn, Co, Ni, Cu, Mo, and Te, and high-field-strength elements (rare earth elements, Ti, Hf, Nb, Ta, and Zr) [1–4]. The geochemical and mineralogical composition of deep-sea Fe–Mn crusts and nodules has been studied to determine the formation processes of manganese nodules [5–10]. Three types of crusts and nodules are usually classified by the predominant genetic process: hydrogenetic, diagenetic, and hydrothermal deposits, which are differentiated by their mineral and elemental compositions [2,11–13]. In contrast to the wealth of information that has been obtained for crusts and nodules found on the sea floor, geochemical, mineralogical, and high-resolution

studies of micro-nodules in carbonate substrate are lacking, despite the occurrence of carbonate rocks at the surfaces of deep-sea floor being well documented [14–20].

Most carbonates in sea water settings are biogenic in origin, covering approximately half of the area of the entire ocean floor [21–23]. The diagenetic processes of carbonate rocks are widespread but complex because of the relatively labile nature of carbonates. Various processes, including gravitational compaction, pressure dissolution, reprecipitation, and cementation, drive the diageneses of carbonate [24]. The diagenetic processes of deep-sea carbonate may alter the geochemical balance between the transportation of calcium, magnesium, trace elements, and manganese in the surrounding environments [21,25–27]. It was reported that the dissolution of foraminiferal tests in the water column might contribute important components to the mineralized source of Fe–Mn crust [28]. Repaid return transportation of seawater from the cavities and fissures of dissolved limestone may also have stimulated Mn deposition during the Barremian–Aptian interval [10]. The deposition of Fe–Mn crust with carbonate cavities and fractures is attributed to the roles of microbes, which act as a specific trap for Fe–Mn ion enrichment [10,27]. The diagenesis of carbonate in tropical water settings was also found to be closely associated with the microbial decomposition of organic matter, which may result in undersaturated pore water with respect to CaCO₃ [29], and the process may be accelerated by the benthic boring fauna [19]. Related microbial processes may involve microbe-driven formation of manganese crust on the seafloor [14,30].

Studies of the carbonate diageneses and formation of Fe–Mn crusts and nodules have been inadequate, especially focusing on the early stage of diageneses. The South China Sea is one of the seas with the largest margins, a deep semi-closed basin, and wide continental shelves in the western Pacific [31,32]. Both carbonate settings and Fe–Mn crust/nodules are well developed [33–37]. Carbonate samples developed with micro-nodules were dredged by a manned submersible Shenhaiyongshi from the Zhaoshu plateau at the Xisha uplift, in the north of the South China Sea (SCS) in July 2019. In this study, mineralogy and geochemical studies on bulk samples and microstructures were conducted to reveal the structure and composition of micro-nodules within carbonate rock, aiming to highlight the relationship between genesis of diagenetic micro-nodules and micritization of carbonates.

2. Geological Setting

In this study, carbonate samples were collected from the Zhaoshu plateau, in the northeast of the Xisha uplift, located along the northwestern continental margin of the SCS (Figure 1A). The Xisha uplift lies in a tectonically dynamic position in the northern SCS and experienced intense block faulting since the rifting and subsequent seafloor spreading of the SCS [38]. Several tropical carbonate platforms, including Yongle, Xuande, Huaguang, Langhua, and Zhaoshu, developed extensively on the Xisha uplift, some of which have been studied extensively with respect to biostratigraphy, lithology, and formation history [33,39–41]. Different drilling results from the Xisha uplift have shown that reef formation initiated in the Eocene–Oligocene transition in limited areas of the southern SCS and spread to wider regions since the early Miocene following accelerated seafloor spreading [39]. Most of the reefs were subsequently drowned when the Xisha uplift subsided during the late Oligocene to early Miocene periods of seafloor spreading [33,42].

The sampling location on Zhaoshu plateau is a flat-topped submarine plateau with a bottom area coverage of ~185 km² and a top area coverage of ~88 km². Geological and petrological studies of this area are lacking, although the location is less than 100 km from Yongxing Island. The depth of the shallowest guyots is about 300–400 m, and that of the adjacent marine basin is about 1300 m (Figure 1B).

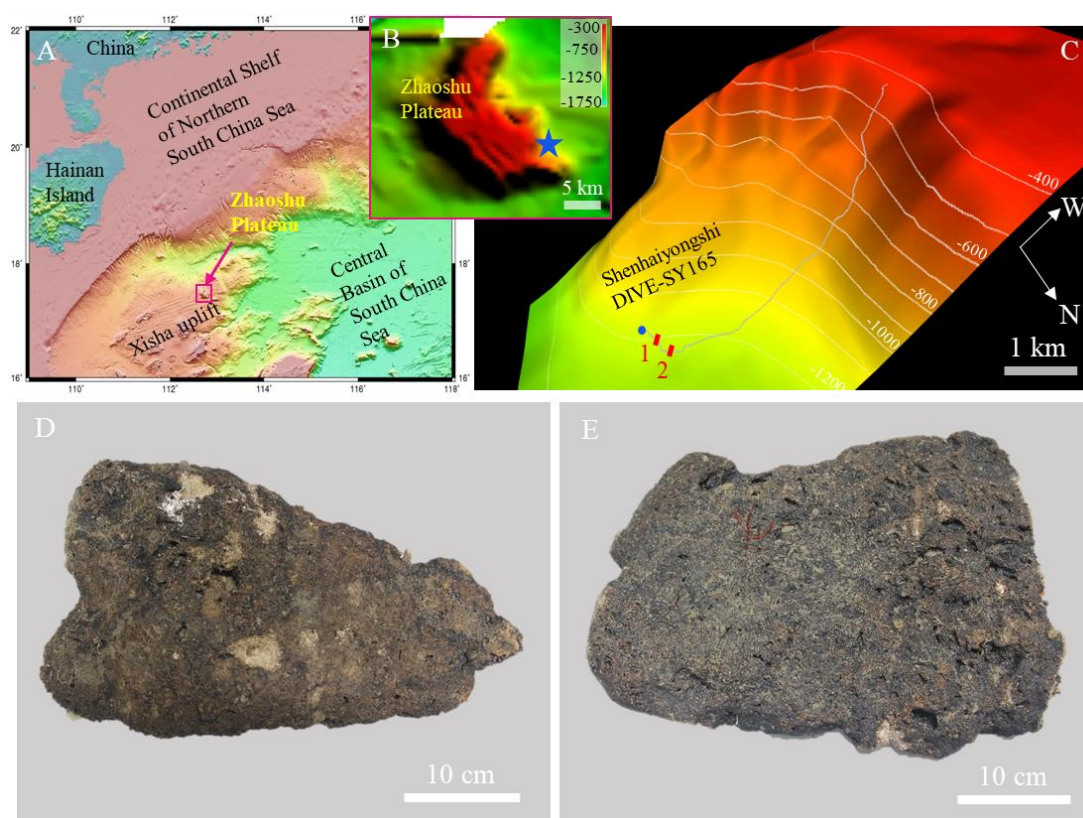


Figure 1. (A) Topography of the northern South China Sea and the location of the investigated area, the Zhaoshu plateau. (B) Enlarged bathymetry of the location of the Zhaoshu plateau. The blue star in the panel indicates the deployment location of Shenhaiyongshi. (C) Dive track on a 3D view of the southeast slope of the Zhaoshu plateau (star in panel B). The blue circular indicates the sampling location, and carbonates developed along to No.1 (shown in Video S1). Carbonate fractures were observed at location No.2 (Video S1). On the way from No. 1 to No. 2, massive sediments were deposited (Figure S1A). (D,E) Two carbonate samples collected by the submersible near the blue circular in (C), which were used in this study.

3. Materials and Methods

3.1. Dives and Sampling

During the TS 12-01 expedition in July 2019, one dive (Dive_SY165, Figure 1C) was performed at the southeast slope of the Zhaoshu plateau by the manned submersible Shenhaiyongshi and the supporting vessel R/V Tansuoyihao, owned by the Institute of Deep-sea Science and Engineering, Chinese Academy of Sciences (IDSSE, CAS, Sanya, China). An external color video camera on the submersible provided video log throughout the dive. Time, depth, and geographic coordinates were overwritten on the high-quality video image, allowing the observation to be located on the submersible's dive track. Carbonate samples were collected by the mechanical arm of the submersible at a water depth of 1171 m at a carbonate formation ($\sim 112.8010^\circ$ E, 17.4245° N; Figure 1C–E, Video S1). When recovered on deck, the carbonate samples were kept at -20°C in a freezer until they were returned to the laboratory for further analysis.

3.2. Laboratory Analyses

Different techniques from bulk to high-resolution in situ analysis were used to determine textural, mineralogical, and geochemical features of the carbonate and inner micro-manganese nodules. X-ray diffraction (XRD) and confocal Raman spectroscopy were performed to determine the mineralogy

of the samples. Geochemical characteristics were obtained from bulk samples. Confocal Raman mapping, scanning electron microscope (SEM), and electron probe micro-analyzer (EPMA) were used to further characterize the micro-nodule and carbonate substrate.

3.2.1. Petrography and Mineralogical Studies

Petrographic analyses of textural and mineralogical features were conducted on polished thin sections (ca. 30–100 μm) using a Leica DM 2700P polarizing light microscope coupled with a DFC550 digital camera (Leica Camera AG, Wetzlar, Germany) at IDSSE. Due to the high abundance of carbonate in present samples, bulk sample XRD cannot effectively discriminate manganic minerals within the micro-manganese nodules. After the bulk mineralogical XRD profiles were acquired, bulk powders were leached by acetate buffer (1 M acetic acid/Na acetate buffer pH 5) to remove carbonate components. The residues were harvested by centrifugation and analyzed twice, after drying at 40 $^{\circ}\text{C}$ and after drying at 105 $^{\circ}\text{C}$ for 24 h [8,43]. The equipment used included a Malvern Panalytical Empyrean X-ray diffractometer at IDSSE. The effective analytical conditions for identifying of micro-nodules were as follows: Cu-K α radiation at 40 kV and 30 mA, a curved graphite secondary monochromator, scan from 5–80 $^{\circ}$ (2 θ), step size of 0.01313 $^{\circ}$ (2 θ), and step time of 0.5 $^{\circ}$ /min.

Confocal Raman spectroscopy was used to support the characterization of these poorly crystalline minerals in the local selected area. Raman analyses were performed on polished thin section by a LabRAM HR Evolution (Horiba Jobin Yvon) confocal Raman spectrometer equipped with a 532 nm excitation laser at IDSSE. We used an optic fiber that was 50 microns in diameter to harvest the inelastically scattered photons. A 100 \times objective was used to provide a spatial resolution between 500 and 360 nm in the Raman images; 600 lines/mm grating was used to obtain spectra with a spectral resolution around 4 cm^{-1} . Raman hyperspectral images of mineral associations were generated by mapping the main peak intensities for specific minerals using the WITec Project alpha300 Rconfocal Raman imaging system (WITec Wissenschaftliche Instrumente und Technologie GmbH, Ulm, Germany) at IDSSE. All Raman peak positions were read directly from the measured average spectra calculated from representative regions with high signal-to-noise ratio (SNR) and after background removal.

3.2.2. Scanning Electron Microscopy and Element Mapping

Micro-nodules from the polished thin sections and freshly fractured carbonate rocks were examined with a ThermoScientific Apreo C SEM equipped with an energy-dispersive X-ray spectroscope and AZtec system provided by Oxford Instruments at IDSSE. The SEM was operated at 2 kV with a working distance of 10 mm to provide optimal imaging and to minimize charging and sample damage in the back-scattered electron imaging mode. An accelerating voltage of 20 kV was used for the X-ray analysis to obtain adequate X-ray counts with a precision of ~5%.

3.2.3. Bulk Geochemical Analysis

The major, minor, and rare earth elements were determined by inductively coupled plasma atomic emission spectroscopy (ICP-AES) and inductively coupled plasma mass spectrometry (ICP-MS) measurements at State Key Laboratory of Marine Geology, Tongji University (Shanghai, China). Samples used for these analyses were dissolved using a solution of HNO_3 + HF on a hot plate. The eluted sample was then diluted with 2% HNO_3 . The analytical precision and accuracy, monitored by the geostandard GSD9 and sample duplicates, were better than 5%.

3.2.4. In Situ Geochemical Analysis by EPMA

EPMA was performed on polished thin sections (ca. 100 μm) to identify elemental distribution in micro-structures of the selected areas. For this, a Jeol JXA-8230 electron probe micro-analyzer (Jeol, Tokyo, Japan) was used at Wuhan Sample Solution Analytical Technology Co. Ltd. (Wuhan, China). Standards were natural minerals from international suppliers. Back-scattered electron images were also obtained with this instrument. We analyzed polished thin sections at a 15 kV

accelerating voltage and a 50 nA beam current. The single layers were analyzed with a focused (1–5 μm) and a defocused (5–20 μm) beam. Counting times for the analyzed elements were 10 s for Mn, Fe, Ni, Cu, Na, Mg, Al, Si, K, Ca, Ti, P, S, and Ba, and 30 s for Co, Mo, Zn, and Pb.

4. Results

4.1. Sea Floor Observation and Carbonates Distribution

The geomorphology of the southeast slope of Zhaoshu plateau, observed by submersible Shenhaiyongshi, is characterized by an evident seabed configuration in which three significant features were identified: a reef-carbonates, pelagic sediments, and outcrops of volcanic rocks (Figure 1A). Carbonate samples collected at the bottom of the plateau were representative of the reef carbonates at water depths between 1171 to 1201 m (Figure 1C). Massive pelagic sediments were deposited on the seafloor between 1067 and 1224 m along the dive track (Figure S1A). Volcanic rocks, including columnar joint blocks and pillow lava, were found in extensive steep outcroppings (460–900 m water depth) (Figure S1B,C). In contrast, dense reef carbonates were found on the top the plateau (Figure S1D). Based on these observations, we concluded that the Zhaoshu plateau might share similar origin models like other platforms and some of the Pacific guyots: prolonged volcanism, followed by subsidence, accumulation of shallow-water reef carbonates, emersion following a sea-level fall, then continued subsidence, erosion, and then drowning [44].

On the seafloor surface of the reference location, the carbonates were like a concrete floor but with cracked fractures (Video S1). Thin and fine grain sediment deposits were observed on the concrete-like seafloor, which were easily disturbed by the submersible propeller. As a result, we were able to distinguish carbonates from massive pelagic sediments. Although large amounts of sediments were identified at water depths between 1201 and 1223 m, the platform erosion was widespread at the edge of the terraces (Video S1).

4.2. Description of Carbonates and Samples

Two carbonate rocks were collected from the fracture of the carbonate deposit (Figure 1D,E). The two rocks were approximately 10 to 16 cm thick. Both were a dull gray color due to the deposition of manganese oxides on their surfaces. The effects of boring by benthic fauna were visible on the rock surface, which enlarged the cavities and fractures in the carbonate. The interiors of the rock were smoky white in color.

Plane vertical cross-sections through the rocks displayed the clear structuring of the carbonates. Skeletal grains of algae and foraminifers were embedded in a calcite muddy matrix, which were fractured, vuggy, and poorly organized (Figure 2). The carbonate samples were mainly composed of accumulations of calcified fragments of coralline algae, some of which had experienced micritization (Figure 2A,C). Most of the algae observed were filled with micrite (Figure 2C,D). In addition, the shells of *Amphistegina* species and other free-living benthic foraminifera significantly contributed to the carbonate rocks (Figure 2B). *Orbulina* sp. and *Sphaeroidinellopsis* were dominant among the planktonic foraminifera species. Other foraminifera occurred in very low numbers. The occurrence of *Orbulina* sp. and *Gq. dehiscens* indicated that the carbonate rocks are 10–16 Ma years old.

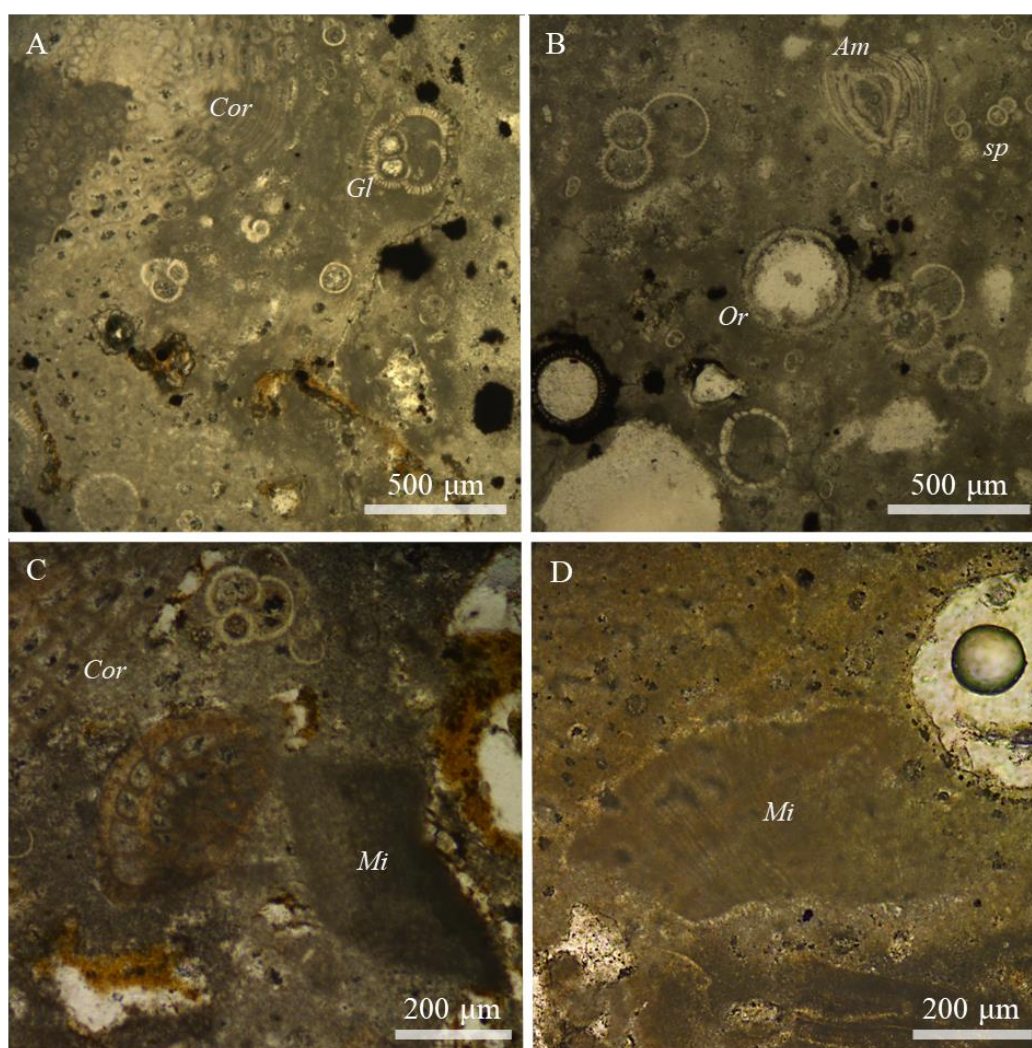


Figure 2. Thin polished section photomicrographs of carbonate rocks from Zhaoshu plateau. (A) Fragments of coralline algae (Cor) and foraminifera species of *Globoquadrina dehiscens* (Gl) in the matrix. (B) Tests of *Amphistegina* species (Am) and other free-living benthic foraminifera like *Orbulina* sp. (Or) in the samples. (C,D) Micritization (Mi) of coralline algae in carbonate.

4.3. Micro-Manganese Nodules in Carbonates: Morphology, Sizes, and Mineralogical Properties

4.3.1. Textures of the Micro-Manganese Nodules

Reflected light microscopy combined with backscatter SEM revealed the morphology and texture of the micro-manganese nodules. In general, nodules showed laminated layering, highlighted by micrometer-thin layers of high and low reflectivity alternating with each other (Figure 3). In the cross-section, nodules with bright layers were classified as having three basic growth habits: (1) concentric growth, (2) botryoidal pattern of laminated oxides, and (3) sub-spherical shape. Some of the Mn oxides were dissimilar to the bright layers but with low reflectivity, especially near the bright micro-nodule layers (Figure 3). Some of the low-reflectivity Mn was also shown to be growing in the shells of fossils (Figure 3G,H). The micro-nodules were mainly 40–100 μm in thickness, sometimes even smaller, and these were embedding into the carbonate matrix. We can easily distinguish nodules at the rock surface and in the inner part from vertical thin sections. In general, the botryoidal pattern of laminated structures was more likely developed at the rock surface. Instead, there was a high probability that concentric and sub-spherical shapes occurred in the inner part.

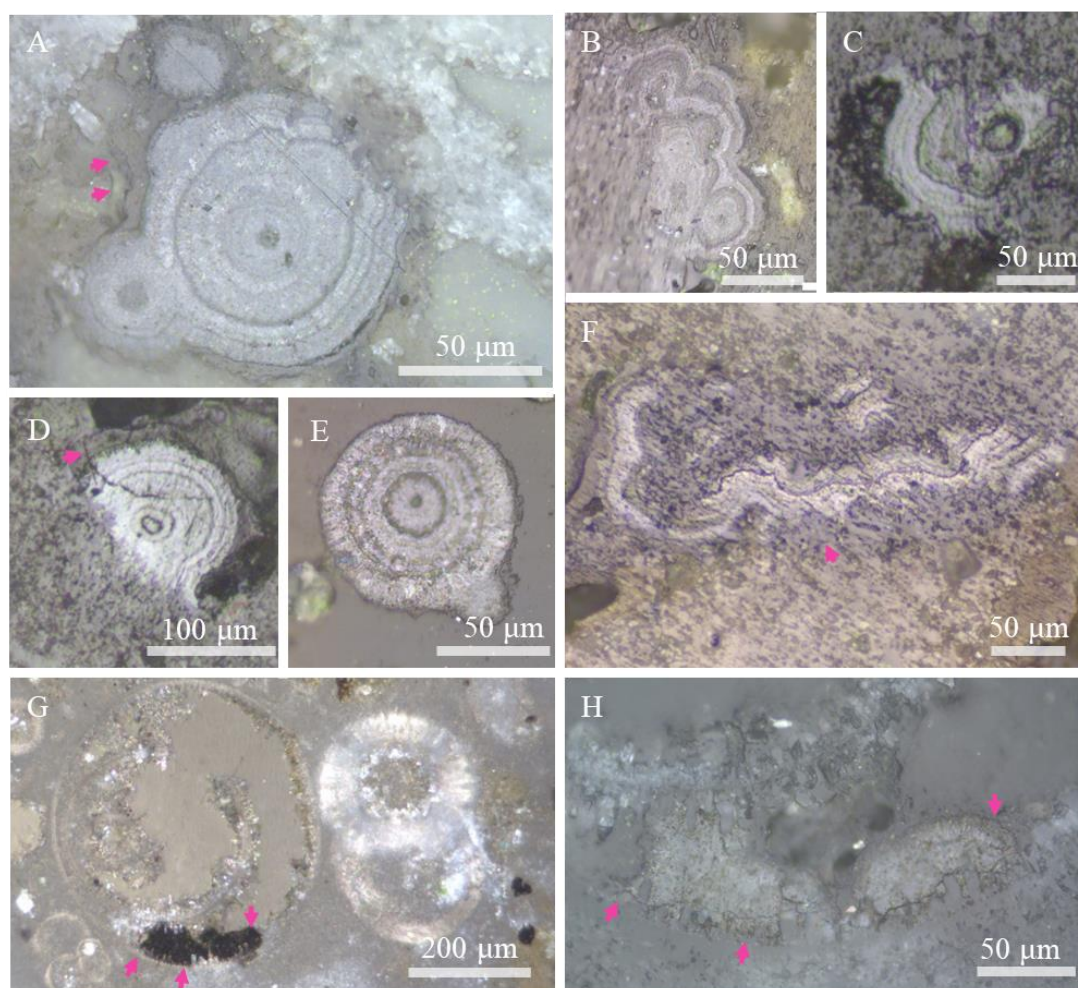


Figure 3. Examples of different Mn mineral textures captured in thin polished section photomicrographs. Concentric growth of nodules (A,E), botryoidal pattern of laminated (B,F), and sub-spherical shape (C,D). Pink arrows indicate that manganic minerals around the micro-nodules were of lower reflectivity compared to the higher reflectivity with the nodules. (G,H) Some of the low-reflectivity manganic minerals growing in a fossil.

SEM images of micro-nodules showed that they were typical phyllo-manganate Mn oxides closely associated with the carbonate substrate within micro-scales (Figure 4). The substrate was fine-scale dense carbonate micrites, on which the typical laminar structure of Mn oxides assembled with laminated or spherical shapes (Figure 4A). The fractured sub-spherical clearly showed the interspace between different layers (Figure 4B,C). Nano- to micro-scale Mn oxides with a laminar shape also filled in the space of the calcite mineral (Figure 4D). The close interactions between carbonate and Mn oxides also could be reflected by the carbonate cements mixed with Mn oxide at the center of the Mn oxide assembly (Figure 4D).

SEM-EDS mapping of micro-nodules with a sub-spherical shape showed that the nodule was rich in Mn, Mg, and Ni (Figure 5). Fe and Co, which are usually rich in marine polymetallic crusts and nodules, were not enriched like Mn, Mg, and Ni because they were unrecognizable between different layers as well as in the interface (Figure 5). In contrast, the distribution of Fe sometimes correlates with the distribution of Si, indicating the mixing of clay minerals (Figure 5). The encrusted micro-nodules in the carbonate substrate were also demonstrated by the elemental distribution of Ca and Mn. The mix of carbonate in micro-nodules was identified by mapping.

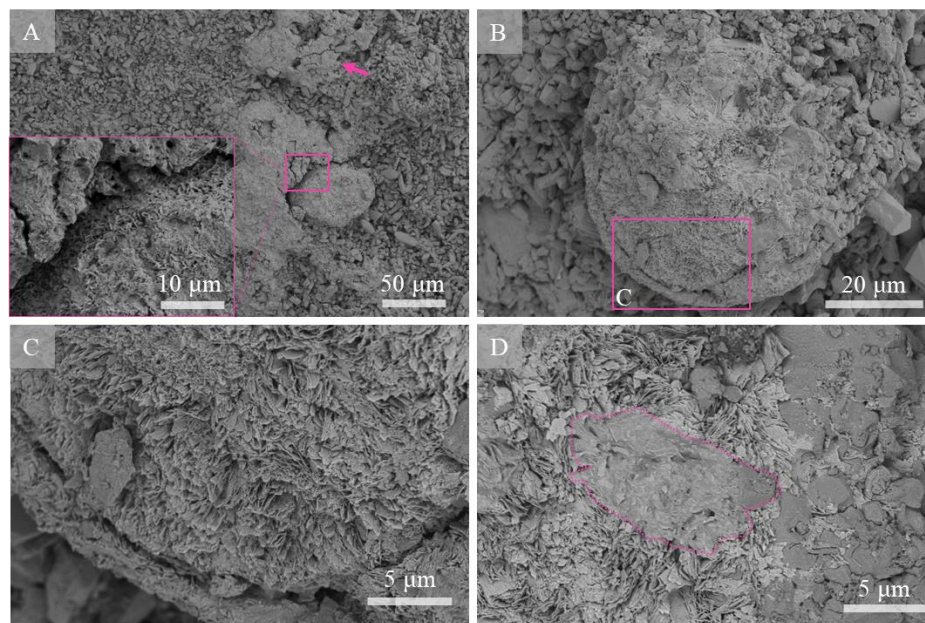


Figure 4. SEM images reveal the distribution of manganese minerals and carbonate micrite. (A) Laminated Mn oxide (arrow) and spherical shapes are encrusted on the micrite. Inset shows that the typical layer structure was well developed in a spherical shape compared with encrusted layers. (B) Sub-spherical Mn oxides commingling with carbonate. (C) Enlarged view of selected area in (B) shows the lamellar shape with clear interface; (D) Mn oxide with laminar shape filled in the space of carbonate. Carbonate cements mixed with Mn oxide at the center of the Mn oxide (dotted outline).

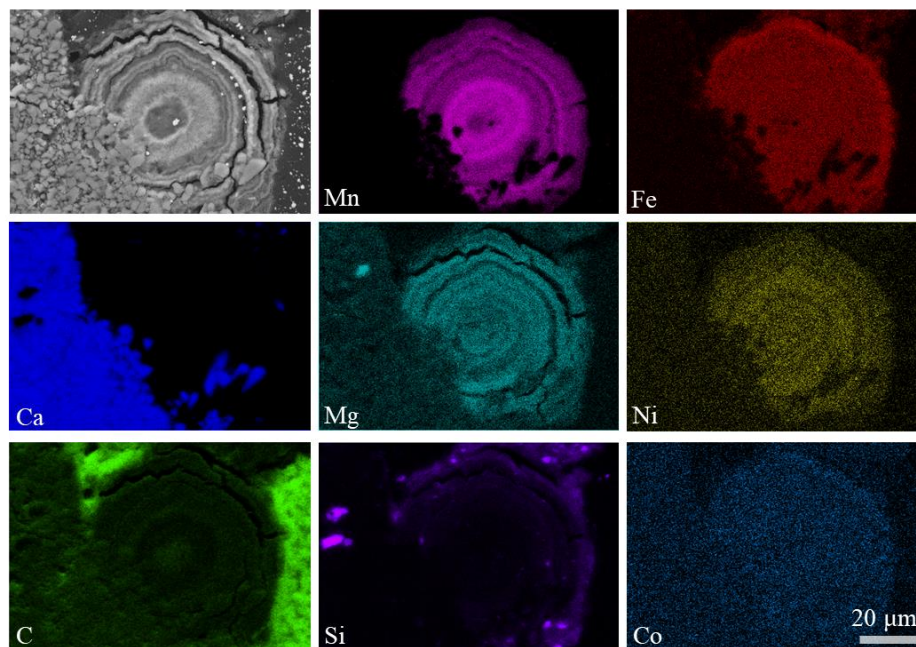


Figure 5. SEM-EDS mapping of different elements within a micro-nodule on a polished thin section. The distribution of Mn perfectly matches that of Ca. The EDS data did not show equal concentration patterns for Mn, Fe, and Co; in contrast to Mn, some Fe concentration was found away from the micro-nodule, but matched with Si. The elemental Mg and Ni were similarly distributed as Mn, while Si was opposite to the gradients of Ca and Mn, having the highest randomly distributed concentration. The distribution of carbon indicated the signature of resin used to prepare the sample.

4.3.2. Mineralogy of the Micro-Manganese Nodules

XRD analyses on bulk samples showed the main patterns of calcite and a low amount of quartz (Figure S2). Owing to the low counts and undefined reflections of Mn oxides in the bulk sample, carbonate components were removed by acetate buffer leaching. Detected minerals in residues were predominantly represented by Mn oxides and detrital minerals (quartz, feldspar, chlorite and muscovite) (Figure 6). The patterns of Mn oxides had diffraction peaks at 10 Å and 7 Å as well as weak peaks at 5 Å and 3.5 Å. The *hk* band at 2.45 Å was overlapped with quartz, and the band at 1.42 Å was not distinguishable, indicating the absence of Fe-vernadite. This pattern is typical for turbostratic phyllosulfates (10 and 7 Å vernadite) [13,43,45–47]. After drying the residues at 105 °C, patterns of major Mn oxides remained at around 10 Å and 7 Å, but with an increase in intensity of 7 Å compared to 10 Å. Collectively, XRD results indicated that micro-nodules in carbonate contained todorokite and 10 Å and 7 Å vernadite.

The local probe of confocal Raman spectroscopy is also used for directly analyzing the local structure of manganese oxides, especially for micro-nodules with poor crystallinity. Three major manganic mineral features were recognized from the Raman shift: (1) broad shoulders at 610–635 cm⁻¹ within the nodule, (2) two peaks at 485–490 and 571–585 cm⁻¹, and (3) weak peaks at 375 cm⁻¹ (Figure 7F). Todorokite in Pacific Fe–Mn nodules was characterized by one intense peak at 610–640 cm⁻¹, which was also comparable to the todorokite from the RRUFF database [48]. In contrast, it is considerably difficult to obtain good identification of 10 and 7 Å vernadite with Raman due to the lack of databases for phyllosulfates in Fe–Mn nodules. The combined XRD and Raman features showed that the micro-nodules were mainly composed of todorokite (Figure 7). In contrast, manganese oxides with low reflectivity near the nodule were characterized by the mixture of calcite micrite and other manganic minerals (Figure 7). The layer of manganese oxides was loose, indicating permeation of epoxy embedding the interspace (Figure 7C).

In order to study the features of mineral distribution around micro-nodules, combined SEM and confocal Raman spectroscopic comparison on fresh fractures were performed. Although the structures of the micro-nodule were not distinguishable from SEM images because they were not on polished thin sections, back-scattered electron images and elemental mapping showed the Mn distribution between the different layers (Figure 8A–C). The substrate showed the clear Raman shift of calcite (280 and 1080 cm⁻¹), which was sometimes closely associated with a low-reflectivity manganic mineral phase (Figure 8D). Compared to the well-developed micro-nodules recognized from the thin sections (Figure 7), the major manganic mineral features of the Raman shift were generally similar to those of the fresh fractures (Figure 8D). Mn phases mixed with calcite micrite sometimes showed high intensity peaks at 490 cm⁻¹ and weak shoulders around 635 cm⁻¹ (Figure 8A). It should be noted that different points within the micro-scale showed a different spectrum on the shoulders and peaks around 635 cm⁻¹ (Figure 8B). Carbonaceous matter (CM) was also detected in some patches of Mn oxides, reflected by the clear D and G bands (Figure 8C). Near the CM, Raman features, like those of the well-developed micro-nodules, were recognized (Figures 7F and 8D).

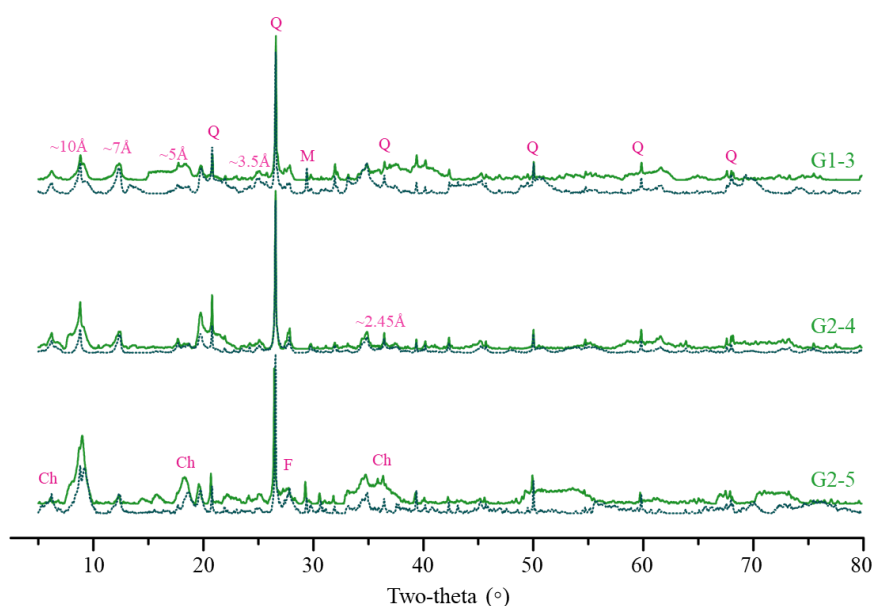


Figure 6. XRD patterns of residual samples after acid leaching. All residual samples were analyzed after drying at 40 °C (solid patterns) and 105 °C (dashed patterns) causing the differences in the diffraction pattern. Other minerals, such as quartz (Q), feldspar (F), chlorite (Ch) and muscovite (M), were labeled near the pattern. Peaks at ~10 Å and ~5 Å are characteristic for 10 Å Mn phases (todorokite/10 Å vernadite). The peaks around ~7 Å are corresponding to 7 Å vernadite. After heating treatment (105 °C/24 h), peaks around ~10 and ~5 Å which are still present but with lower intensity, which are characteristic of stable todorokite phases.

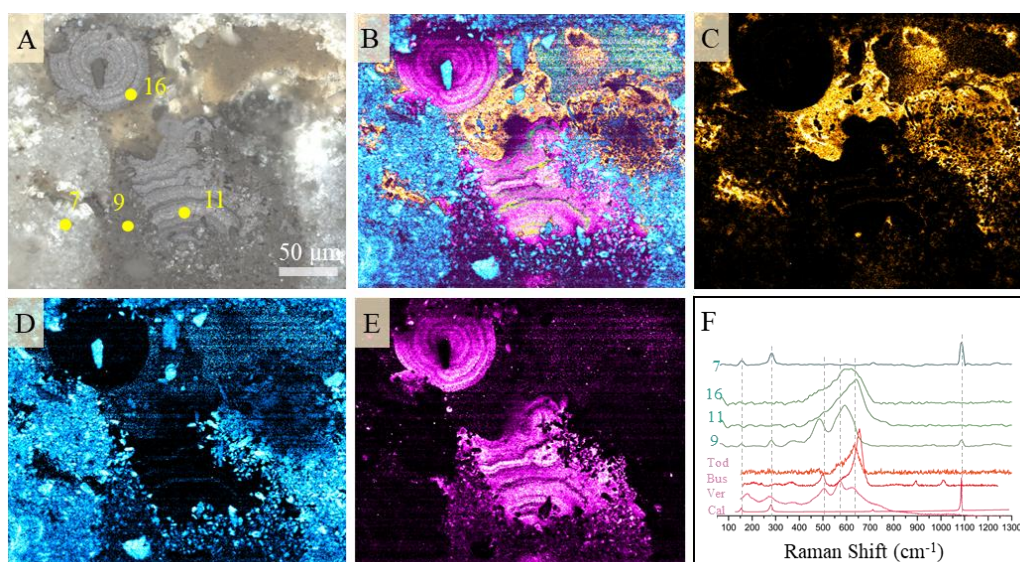


Figure 7. Raman-based probe of mineralogy distribution showing two micro-nodules with sub-spherical shape and laminated shape. (A) Reflected light image of the studied area. Numbers indicate the points where Raman spectra shown in (F) were acquired. (B) Raman mapping distribution of different minerals (components) in the same view of (A). The signature of resin (C), mapping of calcite (D) and manganic minerals (E). (F) Number labels of each Raman spectrum indicate the selected points in (A). Reference spectra of different manganic minerals (todorokite, buserite and vernadite) and calcite from the RRUFF database were used for comparison.

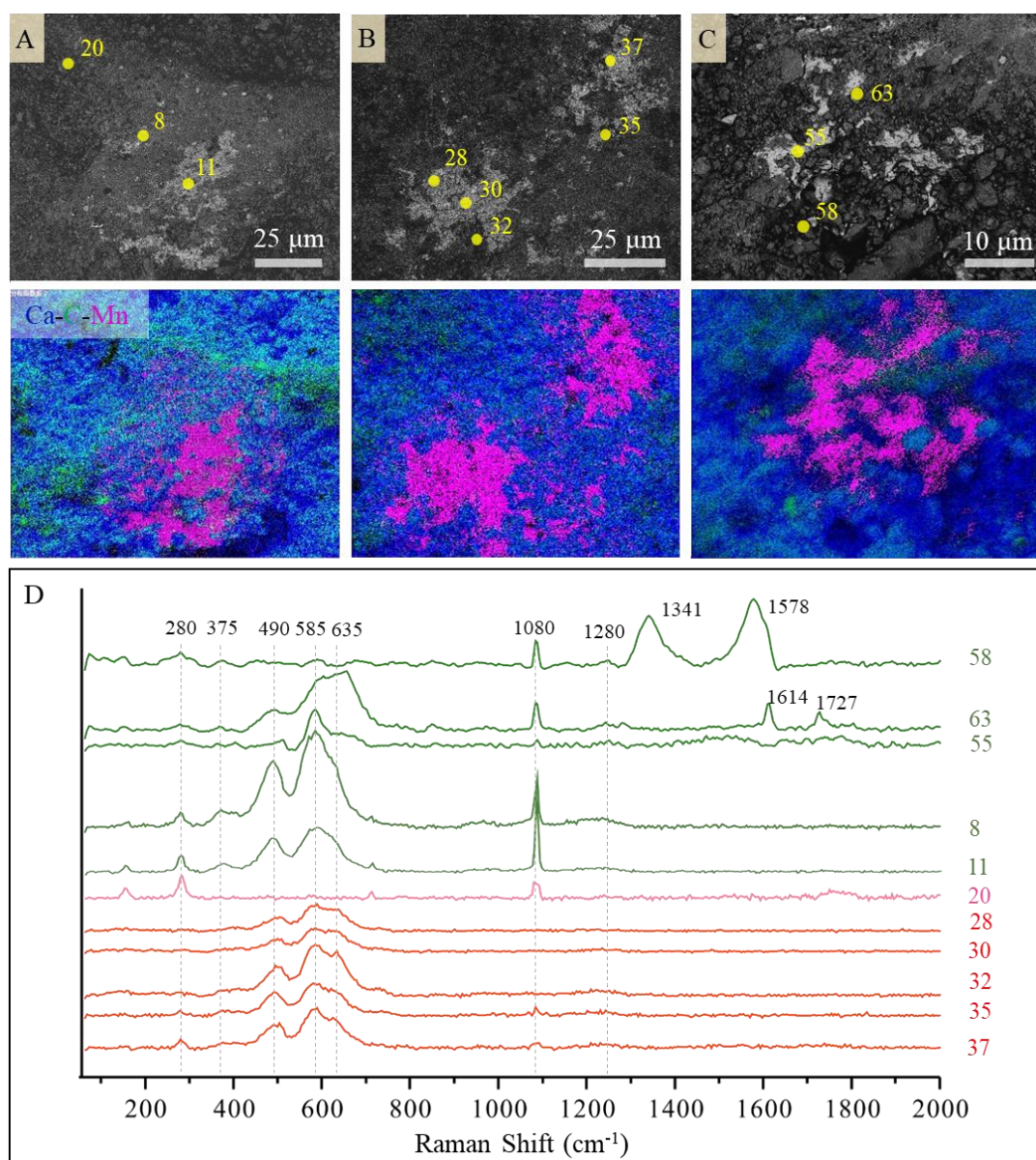


Figure 8. Combined backscattered electron SEM (SEM-BSE) and elemental mapping image and selected area Raman spectra were acquired on three fractured rock samples. (A–C) The upper images show the SEM-BSE images and the lower images show the distribution of Ca, Mn and C in the same area. EDS mapping images were merged in the software Image J. Numbers indicate the points where Raman spectra shown in (D) were acquired.

4.4. Geochemistry

The bulk chemical composition of the carbonate deposits is provided in Table S1. The concentration of CaO, which ranges from 44.97% to 51.67% and reaches negative peak values near the surface of the samples, dominates the Zhaoshu plateau samples' compositional changes. The MgO concentration was no more than 1.53% among all subsamples. The highest MnO concentration was found in subsamples of the dim gray carbonate surface and was up to 2.28%. MnO in the inner subsamples, where micro-nodules were found to be well developed, had relatively lower concentrations (mean 0.70%). Fe₂O₃ content was very low (mean values: inner = 0.70%, outer = 1.64%).

Elements normalized by detrital phase (Al) showed major changes that vary inversely with Ca/Al, reflecting their strong dilution by biogenic calcium (Figure 9A,C). The elemental ratios of REE/Al (rare earth element, REE) were close to the ratio of Mn/Al compared with that of Fe/Al (Figure 9B,D).

The enrichment of REE was largely controlled by the scavenging of Mn (oxyhydr)oxides. The excess of Fe on the outer surface may reflect the Mn oxide scavenging of Fe from the seawater (Figure 9C).

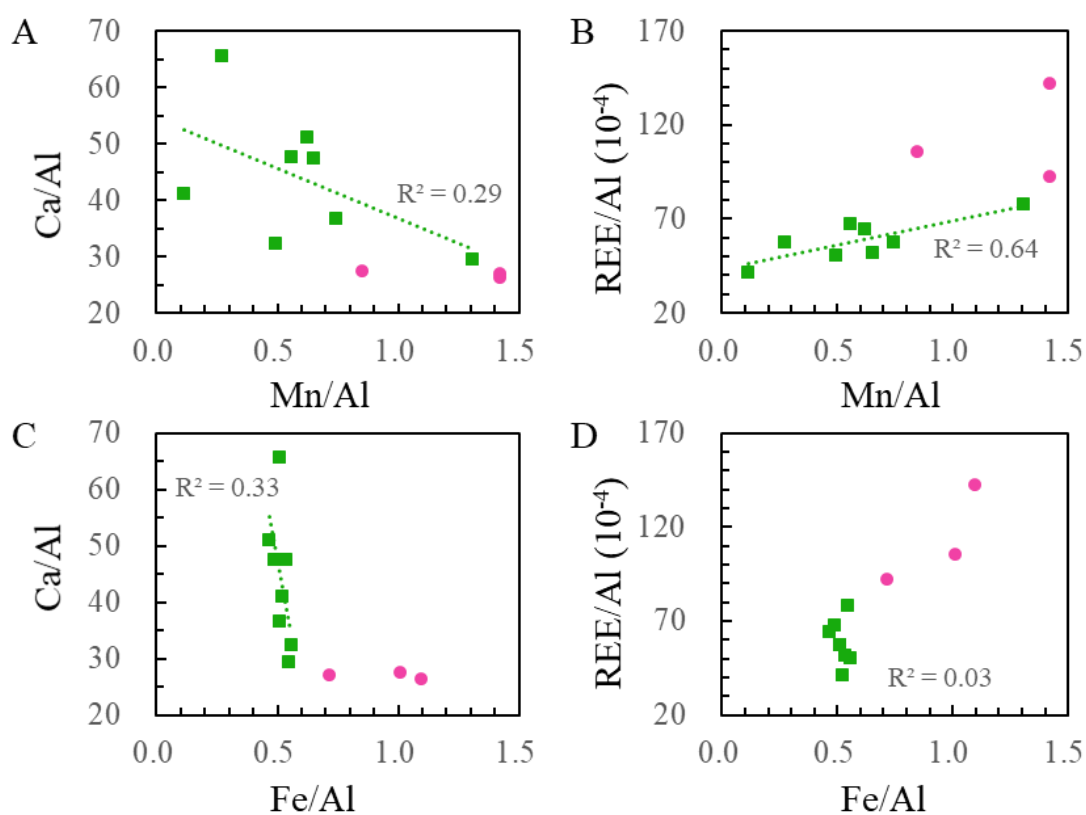


Figure 9. Plots of elemental ratios of inner carbonate (green square) and outer carbonate encrust (pink circle) with a black oxide layer. Mn/Al–Ca/Al (A), Mn/Al–REE/Al (B), Fe/Al–Ca/Al (C) and Fe/Al–REE/Al (D).

EPMA investigation revealed the elemental contents in the micro-nodules (Table 1). Compared to the bulk results, high Mn and low Fe contents were found at the micro-scale. The Mn/Fe ratios showed the highest values in the inner carbonate of up to 116.6 (mean 54.08). The surface of carbonate had lower Mn/Fe values but were higher than five, which is consistent with tendency of bulk samples. The micro-nodules were enriched with metals such as Mg, Ni, Cu, and Zn. The content of Co, which is another transition element in marine polymetallic deposits, was not concentrated, as revealed by the EPMA data and SEM-EDS mapping (Table 1, Figure 5).

Table 1. Average chemical composition in wt.% obtained with the electron probe micro-analyzer (EPMA) of studied Mn oxides and the carbonate matrix.

Sample Name	Mn	Fe	Mn/Fe	Ca	Al	Si	Mg	Cr	Co	Ni	Cu	Zn
Mn encrust at surface (n = 4)	34.62–40.51 37.85	4.27–6.15 4.97	6.59–9.17 7.76	0.69–0.99 0.78	1.31–3.98 2.62	0.73–1.06 0.87	2.80–6.74 4.61	0.03–0.19 0.11	0.06–0.12 0.08	1.17–3.93 2.53	0.30–0.61 0.43	0.15–0.25 0.20
Nodule in the inner (n = 9)	38.59–53.54 45.28	0.41–4.62 1.93	8.40–116.60 54.08	0.78–1.45 1.09	0.55–3.26 1.93	0.09–4.53 0.93	2.61–5.81 4.25	0.05–0.19 0.11	0.07–0.13 0.09	1.37–2.94 2.00	0.50–0.72 0.59	0.16–0.29 0.21
Carbonate matrix (n = 4)	0.004–0.103 0.04	0.003–0.08 0.03	0.28–3.86 1.45	37.98–39.17 38.67	0.004–0.15 0.05	d.l.–0.21 0.14	0.63–0.85 0.72	0.01–0.03 0.02	d.l.–0.02 0.004	d.l.–0.04 0.02	d.l.–0.01 0.009	d.l.

First row, range of concentrations; second row, average values. d.l., below detection limit.

5. Discussion

5.1. Carbonates at the Bottom of the Zhaoshu Plateau

The South China Sea has harbored an extensive number of carbonate platforms and reefs since the late Cenozoic [33]. The Zhaoshu plateau, from which the carbonate samples were collected in this study, belongs to the Xisha uplift; the origins of the carbonates were recognized as the shallow water and biologically controlled deposits [33]. Although few studies considered the carbonate deposits of the Zhaoshu plateau, carbonate plateaus studied at Yongle and Xuande in the northern SCS were adequately characterized by geophysical survey and drilling core analysis carried out to the southwest of the Zhaoshu plateau, no further than 100 km away from the study site. The studied carbonate samples developed in a shallow water environment by reef-building organisms mainly including calcareous algae species, benthic foraminifera, as well as some planktonic foraminiferal species (Figure 2). The recovered samples and near-sea-floor observations along the dive track on the southeast slope showed that the Zhaoshu plateau might have accumulated shallow-water reef carbonates during prolonged volcanism at the bottom. Then, with the intense subsidence and emersion accompanying the sea-level fall, shallow-water carbonate formed at this depth.

The present carbonate samples were mainly characterized by a framework of Corallinaceae, including *Corallina*, *Amphiroa*, and *Lithophyllum*. Calcareous algae, which significantly contribute to reef calcification and cementation, were also reported as the major reef builder at Xisha in the SCS [49,50], Gulf of Suez [51], and the Great Amazon reef [52]. The reef-building coralline algae were claimed to produce massive nodules of up to 10 cm in diameter from thin crusts of only a single-cell thickness, and their building processes led to their extensive representation in the geological records [53]. The distribution of biological species and ecological features of reef-building organisms in the adjacent XK-1 and Chenke-2 in the fossil record revealed that calcareous algae were one of the main builders of the carbonate reef, apart from the corals Corallinaceae, Hapalidiaceae, and Sporolithaceae [54].

The reservoir quality of carbonates was controlled not only by sedimentary facies, but also by the complex sequence of diagenetic processes. Traditionally, processes involved in the diagenetic processes of carbonate diminished the porosity via compaction, dolomitization, anhydritization, micritization, and cementation [51,55–59]. The main diagenetic feature of the present carbonate samples is the massive calcite micrite around bioclasts or partially micritized biological grains (Figure 2). The formation process of the micritic matrix, which was a widespread constituent of carbonate rocks throughout Phanerozoic, is still poorly understood [60]. Carbonate micrite from reefs and carbonate platforms are largely considered derived from the breakdown of biological skeletal grains, such as algae and foraminifers [61,62]. In contrast, the biological skeleton in our samples mainly consisted of coralline algae and chambers of foraminifera. These carbonate reef reservoirs frequently showed complex micritization processes. The occurrence of dense clusters of the micritic matrix as remains of coralline algae provides strong evidence that original carbonates were mostly replaced by micrite calcite.

5.2. Formation of Micro-Manganese Nodules within the Carbonate Matrix

Compared with other Fe–Mn crusts and nodules studied in the SCS, the micro-nodules in the present study were characterized by enrichment of Mn with high Mn/Fe ratios. Marine Fe–Mn oxides can be classified as (1) diagenetic, with Mn/Fe ratios >2.5, being rich in Cu and Ni and poor in Co; (2) hydrogenetic, with Mn/Fe ratios of ~1 and with relatively high concentrations of Co compared to the other genetic types; and (3) hydrothermal, in which Mn/Fe is either very high or very low, characterized by low Cu + Ni + Co content [1,63–65]. Two modified discrimination diagrams [45,63] were used here with a ternary plot of the concentration of Mn, Fe, Co, Ni, and Cu (Figure 10). The bulk carbonate samples, including the outer surface with the Fe–Mn crust, were plotted in the hydrogenetic field, as reported for the Fe–Mn nodules in the northern SCS [37]. However, in situ analysis of micro-nodules by EPMA produced dissimilar discriminations. Figure 10A displays the properties at the edge or outside of the hydrogenetic origin and showed no indicator of hydrothermal origin. According to

the classification, these nodules were typical of a mixed type with early diagenetic growth under oxic–suboxic conditions.

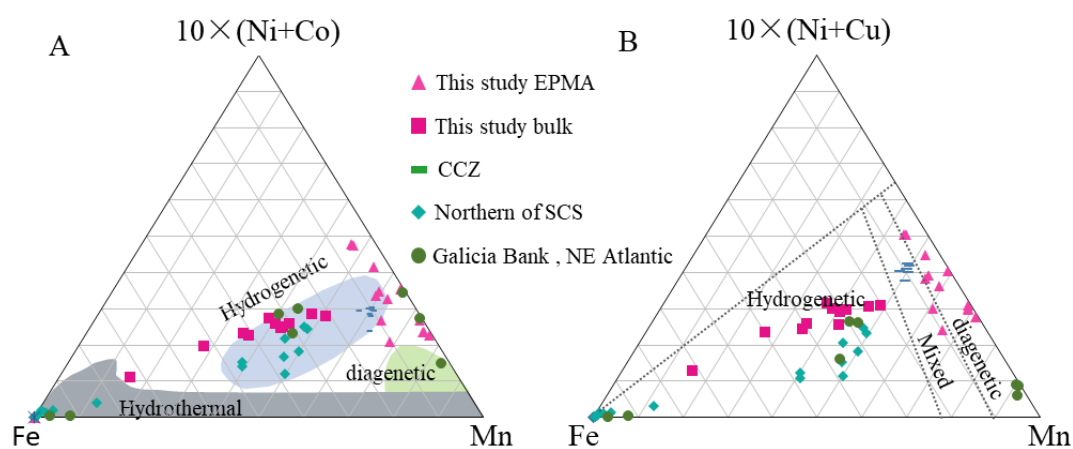


Figure 10. Ternary diagrams of the genetic determination of micro-manganese nodules from the Zhaoshu plateau. Other data were employed for comparison, including the Clarion and Clipperton Zone (CCZ) of the equatorial eastern Pacific [45]; the northern SCS [37]; and the Galicia Bank, Iberian margin, and northeastern Atlantic [66]. (A) Ternary diagram of Fe, Mn, and $(\text{Ni} + \text{Co}) \times 10$; (B) ternary diagram of Fe, Mn and $(\text{Ni} + \text{Cu}) \times 10$. All data in wt.%.

In terms of mineralogy, the diagenetic-type nodule consists of turbostratic phyllosulfates such as 10 \AA vernadite, 7 \AA vernadite and todorokite [13,43,45,46]. 10 \AA vernadite and 7 \AA vernadite were detected by XRD analysis. These two varieties are two-water layer (10 \AA) and one-water layer (7 \AA) of the same type of vernadite, each of which consists of octahedral Mn layers stacked vertically with a constant separation [67]. The formation of turbostratic phyllosulfates was attributed to the metal precipitation from suboxic near-bottom sea water and/or sediment pore water [2,12,13,43,45,46]. Our samples were collected at a water depth of 1200 m, which may have once been shallow during sea subsidence. These depth ranges are closely related to the oxygen minimum zones (OMZ) of the SCS [68], where a favorable reduction of Mn-bearing solid phase occurs [28]. This storage of Mn was not equal to that of Fe (Figure 9) because under such suboxic conditions, Mn^{4+} can be reduced, but no Fe^{3+} reduction occurs [43]. Micro-nodules were usually embedded within the carbonate matrix (Figures 3, 4 and 7). High-resolution SEM showed that Mn oxides with laminated layers and spherical shapes were encrusted on the carbonate micrite (Figure 4). Mn oxides in the inner of carbonate rocks thus may be similar with buried nodules in sediments under oxic and suboxic conditions.

Apart from CaCO_3 , carbonate frameworks such as coralline algae also include Mn oxides, that may participate in the initiation of manganese mineral deposition maintenance [69]. It was reported that the dissolution of carbonate plankton samples may have acted as the main metal source for the growth of Fe–Mn deposits from the seamount area in the Central Pacific [28]. Mn oxides can deposit on the surface of the cell wall as they grow [70–72]. The growth of algae can also concentrate intracellular Mn oxides at low Mn concentrations [71]. During the collapse of the carbonate framework and micritization, released Mn may contribute another important Mn source for growth of micro-nodules. Owing to the source from fossils, these type of nodules seems significantly thinner when compared to other Fe–Mn nodules reported in the South China Sea [35–37,73].

The presence of todorokite, observed by XRD analysis, indicated that the 10 \AA reflection remained conspicuous after heating at $105 \text{ }^\circ\text{C}$ (Figure 6). In situ Raman spectra revealed that nodules with layered growth structures showed preferentially the Raman shift of todorokite ($610\text{--}635 \text{ cm}^{-1}$). The shift of main Raman bands from 635 to 610 cm^{-1} was interpreted as the enlarger of average distances between atoms. The increase in half-bands and decrease in intensity can be recognized as irregular distribution of bond lengths and bond angles of MnO_6 octahedra [48]. Raman results revealed the

changeable of todorokite (Figure 7). We propose Mn oxide in the inner carbonate may transform from phylломanganates to todorokite.

Similar processes in natural environments have reported in nodules under suboxic conditions [5,13,43,45,46,74]. The processes that occurred during the transformation of todorokite from Fe-vernadite were recently concluded [43]. Hydrogenetic Fe-vernadite was firstly dissolved, releasing reduced Mn into pore waters, reacting with more stable 7 Å and 10 Å phylломanganates, and transforming them into todorokite [43]. The transformation is also supported by the high content of magnesium, which is a favorable template ion because of its hydrated diameter close to the tunnel structure of todorokite [43,46,67]. It was concluded that this Mg concentration ranged between 4.1 and 4.9 wt.% [13,67]. The average Mg concentration in micro-nodules was 4.25 wt.% (Table 1) and was related to the Mn within the micro-nodules (Figure 5). The collapse of the carbonate framework and micritization probably contribute the firstly dissolved Mn species in our samples. The Raman shift observed from a small patch of Mn oxides showed highly sensitive D and G bands (Figure 8). Existence of carbonaceous matter may support Mn-reducing heterotrophic microorganisms and produce Mn²⁺. Then, similar todorokite formation processes, such as nodules buried in sediments, may proceed. Consequently, Raman signal of todorokite was noted in association with carbonaceous matter (Figure 8).

6. Conclusions

Our conclusions from this study are as follows:

- (1) Near-sea-floor observations along the southeast slope of the Zhaoshu plateau characterized the sea floor as having an evident seabed configuration, in which three significant features were noted: reef-carbonates, pelagic sediments, and outcrop of volcanic rocks. The geomorphologies indicate intense subsidence and emersion accompanied by sea-level fall of the plateau.
- (2) The main facies of carbonate rocks collected at −1170 m include skeletal grains of algae and foraminifers embedded in a calcite muddy matrix. Micritization is the main diagenetic feature with calcite micrites around bioclasts or partially micritized biological grains.
- (3) Micro-manganese nodules widely developed both at the outer and inner of carbonate rocks but on the micro-scale. The botryoidal pattern of laminated oxides more likely developed at the rock surface. Concentric and sub-spherical shapes formed in the rock with high probability.
- (4) The micro-nodules are mainly composed of 7 and 10 Å vernadite and todorokite, both of which are closely related to carbonate micrite. They were found to have high Mn/Fe ratios and to be enriched in Ni + Cu with low Co contents.
- (5) These micro-nodules are a mixed type with early diagenetic growth under oxic–suboxic conditions. The collapse of the carbonate framework and micritization led to the redistribution of manganite. The reduction of manganite occurred in the inner of carbonate, probably associated with Mn-reducing heterotrophic microorganisms, and then transformed into todorokite in processes similar to those described in buried nodules in sediments.

Supplementary Materials: The following are available online at <http://www.mdpi.com/2075-163X/10/11/1016/s1>. Figure S1: Geomorphology of the southeast slope of the Zhaoshu plateau along the dive track. Numbers at the lower left of each panel indicate water depth. (A) Deimatidae on deep-sea sediments. (B) Fractured volcanic rocks deeper in the water where sediments can be observed. (C) Pillow lava outcrop at the steeper area where few sediments developed. (D) Dense reef carbonates like concrete at the top of the plateau. Figure S2: X-ray powder diffraction diagram of carbonate samples showing the composition main mineral phases. Calcite (rhombus) dominated among all samples. Main patterns of quartz (pentangle) were also recognized. Enlarged view show the manganic mineral features in bulk samples. Table S1: Chemical composition of carbonate rocks collected from the southeast slope of the Zhaoshu plateau. Video S1: Video tapes of sea floor observation along the southeast slope of the Zhaoshu plateau.

Author Contributions: Conceptualization, H.X. and X.P.; formal analysis, H.X.; funding acquisition, X.P.; investigation, H.X., X.P., K.T., J.L., S.C., and M.D.; methodology, H.X., T.S., and Z.Q.; resources, X.P. visualization,

H.X. and T.S.; writing—original draft, H.X.; writing—review and editing, H.X., X.P., K.T., T.S., M.D., J.L., S.C., and Z.Q. All authors have read and agreed to the published version of the manuscript.

Funding: This research was funded by the National Key Research and Development Plan of China, grant number 2017YFC0306702, 2016YFC0304900 and 2018YFC0309802 and the National Science Foundation of China, grant numbers 41906059, 41706046.

Acknowledgments: We are very grateful to the pilots and crew of the Shenhaiyongshi and Tansuoyihao for their professional services during the mission in June and July 2019. The authors are also indebted to Songhai Li, Hanyu Zhang, and Shanya Cai at the IDSSE for their assistance onboard. Furthermore, we gratefully thank the academic editor Carolina Neumann Keim and two anonymous reviewers for providing thoughtful suggestions and comments that significantly helped to improve this paper.

Conflicts of Interest: The authors declare no conflict of interest.

References

1. Hein, J.R.; Koschinsky, A. Deep-ocean ferromanganese crusts and nodules. In *Treatise on Geochemistry*, 2nd ed.; Holland, H.D., Turekian, K.K., Eds.; Elsevier: Oxford, UK, 2014; pp. 273–291.
2. Halbach, F.; Stackelberg, V. The Manganese nodule belt of the Pacific Ocean. *Mineral. Mag.* **1988**, *53*, 664.
3. Roy, S. Environments and processes of manganese deposition. *Econ. Geol. Bull. Soc. Econ. Geol.* **1992**, *87*, 1218–1236. [[CrossRef](#)]
4. Conrad, T.; Hein, J.R.; Paytan, A.; Clague, D.A. Formation of Fe-Mn crusts within a continental margin environment. *Ore Geol. Rev.* **2017**, *87*, 25–40. [[CrossRef](#)]
5. Heller, C.; Kuhn, T.; Versteegh, G.J.M.; Wegorzewski, A.V.; Kasten, S. The geochemical behavior of metals during early diagenetic alteration of buried manganese nodules. *Deep Sea Res. Part I Oceanogr. Res. Pap.* **2018**, *142*, 16–33. [[CrossRef](#)]
6. Johnson, J.E.; Webb, S.M.; Ma, C.; Fischer, W.W. Manganese mineralogy and diagenesis in the sedimentary rock record. *Geochim. Cosmochim. Acta* **2016**, *173*, 210–231. [[CrossRef](#)]
7. Takahashi, Y.; Manceau, A.; Geoffroy, N.; Marcus, M.A.; Usui, A. Chemical and structural control of the partitioning of Co, Ce, and Pb in marine ferromanganese oxides. *Geochim. Cosmochim. Acta* **2007**, *71*, 984–1008. [[CrossRef](#)]
8. Uspenskaya, T.Y.; Gorshkov, A.I.; Sivtsov, A.V. Mineralogy and internal structure of Fe-Mn nodules from the Clarion-Clipperton Zone. *Int. Geol. Rev.* **1987**, *29*, 363–371. [[CrossRef](#)]
9. Lugović, B.; Segvić, B.; Šegvić, T. Mn-crust todorokite mineralization on SW backshore Cretaceous limestones from the island of Dugi Otok (Central Adriatic, Croatia). *Acta Adriat.* **2008**, *49*, 53–63.
10. Rojković, I.; Aubrecht, R.; Mišić, M. Mineral and chemical composition of manganese hardgrounds in Jurassic limestones of the Western Carpathians. *Geol. Carpathica* **2003**, *54*, 317–328.
11. Marino, E.; Gonzalez, F.J.; Kuhn, T.; Madureira, P.; Wegorzewski, A.V.; Mirao, J.; Medialdea, T.; Oeser, M.; Miguel, C.; Reyes, J.; et al. Hydrogenetic, diagenetic and hydrothermal processes forming ferromanganese crusts in the Canary Island Seamounts and their influence in the metal recovery rate with hydrometallurgical methods. *Minerals* **2019**, *9*, 439. [[CrossRef](#)]
12. Koschinsky, A.; Halbach, P. Sequential leaching of marine ferromanganese precipitates: Genetic implications. *Geochim. Cosmochim. Acta* **1995**, *59*, 5113–5132. [[CrossRef](#)]
13. Wegorzewski, A.; Kuhn, T.; Dohrmann, R.; Wirth, R.; Grangeon, S. Mineralogical characterization of individual growth structures of Mn-nodules with different Ni+Cu content from the central Pacific Ocean. *Am. Mineral.* **2015**, *100*, 2497–2508. [[CrossRef](#)]
14. Christ, N.; Immenhauser, A.; Wood, R.A.; Darwich, K.; Niedermayr, A. Petrography and environmental controls on the formation of Phanerozoic marine carbonate hardgrounds. *Earth-Sci. Rev.* **2015**, *151*, 176–226. [[CrossRef](#)]
15. Conti, M.A.; Girasoli, D.E.; Frezza, V.; Conte, A.M.; Martorelli, E.; Matteucci, R.; Chiocci, F.L. Repeated events of hardground formation and colonisation by endo-epilithozoans on the sediment-starved Pontine continental slope (Tyrrhenian Sea, Italy). *Mar. Geol.* **2013**, *336*, 184–197. [[CrossRef](#)]
16. Wheeler, A.J.; Stadnitskaia, A. Benthic Deep-Sea Carbonates: Reefs and Seeps. In *Developments in Sedimentology*; HüNeke, H., Mulder, T., Eds.; Elsevier: Amsterdam, The Netherlands, 2011; pp. 397–455.
17. Noé, S.; Titschack, J.; Freiwald, A.; Dullo, W.-C. From sediment to rock: Diagenetic processes of hardground formation in deep-water carbonate mounds of the NE Atlantic. *Facies* **2006**, *52*, 183–208. [[CrossRef](#)]

18. Aghib, F.S.; Bernoulli, D.; Weissert, H. Hardground formation in the Bannock Basin, Eastern Mediterranean. *Mar. Geol.* **1991**, *100*, 103–113. [[CrossRef](#)]
19. Xu, H.; Peng, X.; Chen, S.; Li, J.; Dasgupta, S.; Ta, K.; Du, M. Macrofaunal burrowing enhances deep-sea carbonate lithification on the Southwest Indian Ridge. *Biogeosciences* **2018**, *15*, 6387–6397. [[CrossRef](#)]
20. Guptha, M.V.S.; Banerjee, R.; Mergulhao, L. On the nature of the calcareous substrate of a ferromanganese crust from the Vityaz Fracture Zone, Central Indian Ridge: Inferences on paleoceanography. *Geo-Marine Lett.* **2002**, *22*, 12–18.
21. Yu, J.; Anderson, R.F.; Rohling, E.J. Deep ocean carbonate chemistry and glacial-interglacial atmospheric CO₂ changes. *Oceanography* **2014**, *27*, 16–25. [[CrossRef](#)]
22. Schlager, W. Carbonate sedimentology and sequence stratigraphy. In *SEPM Concepts in Sedimentology and Paleontology*; Society for Sedimentary Geology (SEPM): Tulsa, Ok, USA, 2005.
23. Ridgwell, A.; Zeebe, R.E. The role of the global carbonate cycle in the regulation and evolution of the Earth system. *Earth Planet. Sci. Lett.* **2005**, *234*, 299–315. [[CrossRef](#)]
24. Croizé, D.; Renard, F.; Gratier, J.-P. Compaction and porosity reduction in carbonates: A review of observations, theory, and experiments. *Adv. Geophys.* **2013**, *54*, 181–238.
25. Rae, J.W.B.; Foster, G.L.; Schmidt, D.N.; Elliott, T. Boron isotopes and B/Ca in benthic foraminifera: Proxies for the deep ocean carbonate system. *Earth Planet. Sci. Lett.* **2011**, *302*, 403–413. [[CrossRef](#)]
26. Holligan, P.M.; Robertson, J.E. Significance of ocean carbonate budgets for the global carbon cycle. *Glob. Chang. Biol.* **1996**, *2*, 85–95. [[CrossRef](#)]
27. Reolid, M. Palaeoenvironmental contexts for microbial communities from Fe-Mn crusts of Middle-Upper Jurassic hardgrounds (Betic-Rifian Cordillera). *Rev. Esp. Paleontol.* **2011**, *26*, 135–160. [[CrossRef](#)]
28. Halbach, P.; Puteanus, D. The influence of the carbonate dissolution rate on the growth and composition of Co-rich ferromanganese crusts from Central Pacific Seamount Areas. *Earth Planet. Sci. Lett.* **1984**, *68*, 73–87. [[CrossRef](#)]
29. Berner, R.A.; Westrich, J.T.; Graber, R.; Smith, J.; Martens, C.S. Inhibition of aragonite precipitation from supersaturated seawater; a laboratory and field study. *Am. J. Sci.* **1978**, *278*, 816–837. [[CrossRef](#)]
30. Konhauser, K.O. Diversity of bacterial iron mineralization. *Earth-Sci. Rev.* **1998**, *43*, 91–121. [[CrossRef](#)]
31. Taylor, B.; Hayes, D.E. The Tectonic Evolution of the South China Basin. In *The Tectonic and Geologic Evolution of Southeast Asian Seas and Islands*; Hayes, D.E., Ed.; American Geophysical Union: Washington, DC, USA, 1980; pp. 89–104.
32. Ru, K.; Pigott, J.D. Episodic rifting and subsidence in the South China Sea. *AAPG Bull.* **1986**, *70*, 1136–1155.
33. Wu, S.; Yang, Z.; Wang, D.; Lü, F.; Lüdmann, T.; Fulthorpe, C.; Wang, B. Architecture, development and geological control of the Xisha carbonate platforms, northwestern South China Sea. *Mar. Geol.* **2014**, *350*, 71–83. [[CrossRef](#)]
34. Shen, J.; Wang, Y. Modern microbialites and their environmental significance, Meiji reef atoll, Nansha (Spratly) Islands, South China Sea. *Sci. China Ser. D Earth Sci.* **2008**, *51*, 608–617. [[CrossRef](#)]
35. Zhong, Y.; Liu, Q.; Chen, Z.; González, F.J.; Hein, J.R.; Zhang, J.; Zhong, L. Tectonic and paleoceanographic conditions during the formation of ferromanganese nodules from the northern South China Sea based on the high-resolution geochemistry, mineralogy and isotopes. *Mar. Geol.* **2019**, *410*, 146–163. [[CrossRef](#)]
36. Jiang, X.; Sun, X.; Guan, Y. Biogenic mineralization in the ferromanganese nodules and crusts from the South China Sea. *J. Asian Earth Sci.* **2019**, *171*, 46–59. [[CrossRef](#)]
37. Zhong, Y.; Chen, Z.; González, F.J.; Hein, J.R.; Zheng, X.; Li, G.; Luo, Y.; Mo, A.; Tian, Y.; Wang, S. Composition and genesis of ferromanganese deposits from the northern South China Sea. *J. Asian Earth Sci.* **2017**, *138*, 110–128. [[CrossRef](#)]
38. Gao, J.; Bangs, N.; Wu, S.; Cai, G.; Han, S.; Ma, B.; Wang, J.; Yangbing, X.; Huang, W.; Dong, D.; et al. Post-seafloor spreading magmatism and associated magmatic hydrothermal systems in the Xisha uplift region, northwestern South China Sea. *Basin Res.* **2019**, *31*, 688–708. [[CrossRef](#)]
39. Shao, L.; Li, Q.; Zhu, W.; Zhang, D.; Qiao, P.; Liu, X.; You, L.; Cui, Y.; Dong, X. Neogene carbonate platform development in the NW South China Sea: Litho-, bio- and chemo-stratigraphic evidence. *Mar. Geol.* **2017**, *385*, 233–243. [[CrossRef](#)]
40. Zhu, W.; Xie, X.; Wang, Z.; Zhang, D.; Zhang, C.; Cao, L.; Shao, L. New insights on the origin of the basement of the Xisha Uplift, South China Sea. *Sci. China Earth Sci.* **2017**, *60*, 2214–2222. [[CrossRef](#)]

41. Yu, K. Coral reefs in the South China Sea: Their response to and records on past environmental changes. *Sci. China Earth Sci.* **2012**, *55*, 1217–1229. [[CrossRef](#)]
42. Hutchison, C.S. Marginal basin evolution: The southern South China Sea. *Mar. Pet. Geol.* **2004**, *21*, 1129–1148. [[CrossRef](#)]
43. Wegorzewski, A.V.; Grangeon, S.; Webb, S.M.; Heller, C.; Kuhn, T. Mineralogical transformations in polymetallic nodules and the change of Ni, Cu and Co crystal-chemistry upon burial in sediments. *Geochim. Cosmochim. Acta* **2020**, *282*, 19–37. [[CrossRef](#)]
44. Flood, P. Development of northwest Pacific guyots: General results from Ocean Drilling Program legs 143 and 144. *Isl. Arc* **1999**, *8*, 92–98. [[CrossRef](#)]
45. Wegorzewski, A.V.; Kuhn, T. The influence of suboxic diagenesis on the formation of manganese nodules in the Clarion Clipperton nodule belt of the Pacific Ocean. *Mar. Geol.* **2014**, *357*, 123–138. [[CrossRef](#)]
46. Manceau, A.; Lanson, M.; Takahashi, Y. Mineralogy and crystal chemistry of Mn, Fe, Co, Ni, and Cu in a deep-sea Pacific polymetallic nodule. *Am. Mineral.* **2014**, *99*, 2068–2083. [[CrossRef](#)]
47. Peacock, C.L.; Sherman, D.M. Sorption of Ni by birnessite: Equilibrium controls on Ni in seawater. *Chem. Geol.* **2007**, *238*, 94–106. [[CrossRef](#)]
48. Ostrooumov, M. Raman and Infrared Reflection Spectroscopic Study of Mineralogical Composition of Iron-Manganese Nodules (Pacific and Indian Oceans). *Int. J. Exp. Spectrosc. Tech.* **2017**, *2*, 2–12. [[CrossRef](#)]
49. Ma, Z.; Zhu, Y.; Liu, X.; Luo, W.; Ma, R.; Xu, S. Quaternary calcareous alga and its ecological function from the ZK-1 well in Xisha Islands. *Earth Sci.-J. China Univ. Geosci.* **2015**, *40*, 718–724. (In Chinese with English abstract)
50. Luo, W.; Zhang, D.; Liu, X.; Wang, Z.; Hu, W.; Wang, Y. A comprehensive stratigraphic study of well XK-1 in the Xiasha area. *J. Stratigr.* **2018**, *42*, 485–498. (In Chinese with English abstract)
51. Sallam, E.S.; Afife, M.M.; Fares, M.; van Loon, A.J.; Ruban, D.A. Sedimentary facies and diagenesis of the Lower Miocene Rudeis Formation (southwestern offshore margin of the Gulf of Suez, Egypt) and implications for its reservoir quality. *Mar. Geol.* **2019**, *413*, 48–70. [[CrossRef](#)]
52. Francini-Filho, R.B.; Asp, N.E.; Eduardo, S.; John, H.; Kenneth, L.; Nilo, D.A.; Vasconcelos, A.A.; Ricardo, B.; Rezende, C.E.; Omachi, C.Y. Perspectives on the Great Amazon Reef: Extension, biodiversity, and threats. *Front. Mar. Sci.* **2018**, *5*, 142. [[CrossRef](#)]
53. Ries, J.B. Mg fractionation in crustose coralline algae: Geochemical, biological, and sedimentological implications of secular variation in the Mg/Ca ratio of seawater. *Geochim. Cosmochim. Acta* **2006**, *70*, 891–900. [[CrossRef](#)]
54. Li, Y.; Yu, K.; Wang, Y.; Wang, R.; Fan, T.; Bian, L. The composition of coralline algae from well Chenke-2 Xisha Islands South China Sea and its implication on the water depth. *Acta Micropalaeontol. Sin.* **2017**, *34*, 268–278. (In Chinese with English abstract).
55. Moore, C.H.; Wade, W.J. Carbonate diagenesis: Introduction and tools. In *Developments in Sedimentology*; Moore, C.H., Wade, W.J., Eds.; Elsevier: Amsterdam, The Netherlands, 2013; pp. 67–89.
56. Flügel, E. Diagenesis, porosity, and dolomitization. In *Microfacies of Carbonate Rocks*; Springer: Berlin/Heidelberg, Germany, 2004; pp. 267–338.
57. Moore, C.H. *Carbonate Diagenesis and Porosity*; Elsevier: Amsterdam, The Netherlands, 1989.
58. Wanless, H.R. Burial diagenesis in limestones. In *Sediment Diagenesis*; Parker, A., Sellwood, B.W., Eds.; Springer: Dordrecht, The Netherlands, 1983; pp. 379–417.
59. Cook, H.E.; Egbert, R.M. Diagenesis of deep-sea carbonates. In *Developments in Sedimentology*; Larsen, G., Chilingar, G.V., Eds.; Elsevier: Amsterdam, The Netherlands, 1979; pp. 213–288.
60. Vodrazkova, S.; Munnecke, A. Calcispheres as a source of lime mud and peloids evidence from the early Middle Devonian of the Prague Basin, the Czech Republic. *Bull. Geosci.* **2010**, *85*, 585–602.
61. Gischler, E.; Dietrich, S.; Harris, D.; Webster, J.M.; Ginsburg, R.N. A comparative study of modern carbonate mud in reefs and carbonate platforms: Mostly biogenic, some precipitated. *Sediment. Geol.* **2013**, *292*, 36–55. [[CrossRef](#)]
62. Enríquez, S.; Schubert, N. Direct contribution of the seagrass *Thalassia testudinum* to lime mud production. *Nat. Commun.* **2014**, *5*, 3835. [[CrossRef](#)]
63. Fu, Y.; Wen, H. Variabilities and enrichment mechanisms of the dispersed elements in marine Fe–Mn deposits from the Pacific Ocean. *Ore Geol. Rev.* **2020**, *121*, 103470. [[CrossRef](#)]

64. Guan, Y.; Sun, X.; Jiang, X.; Sa, R.; Zhou, L.; Huang, Y.; Liu, Y.; Li, X.; Lu, R.; Wang, C. The effect of Fe-Mn minerals and seawater interface and enrichment mechanism of ore-forming elements of polymetallic crusts and nodules from the South China Sea. *Acta Oceanol. Sin.* **2017**, *36*, 34–46. [[CrossRef](#)]
65. Hein, J.R.; Schulz, M.S.; Dunham, R.E.; Stern, R.J.; Bloomer, S.H. Diffuse flow hydrothermal manganese mineralization along the active Mariana and southern Izu-Bonin arc system, western Pacific. *J. Geophys. Res. Solid Earth* **2008**, *113*, B08S14. [[CrossRef](#)]
66. Gonzalez, F.J.; Somoza, L.; Hein, J.R.; Medialdea, T.; Leon, R.; Urgorri, V.; Reyes, J.; Martin-Rubi, J.A. Phosphorites, Co-rich Mn nodules, and Fe-Mn crusts from Galicia Bank, NE Atlantic: Reflections of Cenozoic tectonics and paleoceanography. *Geochem. Geophys. Geosyst.* **2016**, *17*, 346–374. [[CrossRef](#)]
67. Bodeï, S.; Manceau, A.; Geoffroy, N.; Baronnet, A.; Buatier, M. Formation of todorokite from vernadite in Ni-rich hemipelagic sediments. *Geochim. Cosmochim. Acta* **2007**, *71*, 5698–5716. [[CrossRef](#)]
68. Li, L.; Qu, T. Thermohaline circulation in the deep South China Sea basin inferred from oxygen distributions. *J. Geophys. Res. Ocean.* **2006**, *111*, C05017. [[CrossRef](#)]
69. Wang, X.-H.; Schloßmacher, U.; Natalio, F.; Schröder, H.C.; Wolf, S.E.; Tremel, W.; Müller, W.E.G. Evidence for biogenic processes during formation of ferromanganese crusts from the Pacific Ocean: Implications of biologically induced mineralization. *Micron* **2009**, *40*, 526–535. [[CrossRef](#)]
70. Chaput, D.L.; Fowler, A.J.; Seo, O.; Duhn, K.; Hansel, C.M.; Santelli, C.M. Mn oxide formation by phototrophs: Spatial and temporal patterns, with evidence of an enzymatic superoxide-mediated pathway. *Sci. Rep.* **2019**, *9*, 18244. [[CrossRef](#)] [[PubMed](#)]
71. Knauer, K.; Jabusch, T.; Sigg, L. Manganese uptake and Mn(II) oxidation by the alga *Scenedesmus subspicatus*. *Aquat. Sci.* **1999**, *61*, 44–58. [[CrossRef](#)]
72. Schöler, A.; Zaharieva, I.; Zimmermann, S.; Wiechen, M.; Manke, A.-M.; Kurz, P.; Plieth, C.; Dau, H. Biogenic manganese–calcium oxides on the cell walls of the algae *Chara Corallina*: Elemental composition, atomic structure, and water-oxidation catalysis. *Eur. J. Inorg. Chem.* **2014**, *2014*, 780–790. [[CrossRef](#)]
73. Guan, Y.; Sun, X.; Ren, Y.; Jiang, X. Mineralogy, geochemistry and genesis of the polymetallic crusts and nodules from the South China Sea. *Ore Geol. Rev.* **2017**, *89*, 206–227. [[CrossRef](#)]
74. Uramoto, G.-I.; Morono, Y.; Tomioka, N.; Wakaki, S.; Nakada, R.; Wagai, R.; Uesugi, K.; Takeuchi, A.; Hoshino, M.; Suzuki, Y.; et al. Significant contribution of subseafloor microparticles to the global manganese budget. *Nat. Commun.* **2019**, *10*, 400. [[CrossRef](#)] [[PubMed](#)]

Publisher’s Note: MDPI stays neutral with regard to jurisdictional claims in published maps and institutional affiliations.



© 2020 by the authors. Licensee MDPI, Basel, Switzerland. This article is an open access article distributed under the terms and conditions of the Creative Commons Attribution (CC BY) license (<http://creativecommons.org/licenses/by/4.0/>).